



HAL
open science

Spectroscopy and efficient laser operation around 2.8 μm of Er:(Lu,Sc)2O3 sesquioxide ceramics

Liza Basyrova, Pavel Loiko, Wei Jing, Yicheng Wang, Hui Huang, Elena Dunina, Alexey Kornienko, Liudmila Fomicheva, Bruno Viana, Uwe Griebner,
et al.

► To cite this version:

Liza Basyrova, Pavel Loiko, Wei Jing, Yicheng Wang, Hui Huang, et al.. Spectroscopy and efficient laser operation around 2.8 μm of Er:(Lu,Sc)2O3 sesquioxide ceramics. Journal of Luminescence, 2021, 240, pp.118373. 10.1016/j.jlumin.2021.118373 . hal-03345626

HAL Id: hal-03345626

<https://hal.science/hal-03345626>

Submitted on 18 Nov 2022

HAL is a multi-disciplinary open access archive for the deposit and dissemination of scientific research documents, whether they are published or not. The documents may come from teaching and research institutions in France or abroad, or from public or private research centers.

L'archive ouverte pluridisciplinaire **HAL**, est destinée au dépôt et à la diffusion de documents scientifiques de niveau recherche, publiés ou non, émanant des établissements d'enseignement et de recherche français ou étrangers, des laboratoires publics ou privés.

Spectroscopy and efficient ~2.8 μm laser operation of Er:(Lu,Sc)₂O₃ sesquioxide ceramics

Liza Basyrova^a, Pavel Loiko^a, Wei Jing^b, Yicheng Wang^c, Hui Huang^b, Elena Dunina^d, Alexey Kornienko^d, Liudmila Fomicheva^e, Bruno Viana^f, Uwe Griebner^c, Valentin Petrov^c, Magdalena Aguiló^g, Francesc Díaz^g, Xavier Mateos^{g,h}, and Patrice Camy^{a,*}

^a*Centre de Recherche sur les Ions, les Matériaux et la Photonique (CIMAP), UMR 6252 CEA-CNRS-ENSICAEN, Université de Caen Normandie, 6 Boulevard du Maréchal Juin, 14050 Caen Cedex 4, France*

^b*Institute of Chemical Materials, China Academy of Engineering Physics, 64 Mianshan Road, 621900 Mianyang, China*

^c*Max Born Institute for Nonlinear Optics and Short Pulse Spectroscopy, Max-Born-Str. 2a, 12489 Berlin, Germany*

^d*Vitebsk State Technological University, 72 Moskovskaya Ave., 210035 Vitebsk, Belarus*

^e*Belarusian State University of Informatics and Radioelectronics, 6 Brovki St., 220027, Minsk, Belarus*

^f*Chimie ParisTech, PSL University, CNRS, Institut de Recherche de Chimie Paris, 11 rue Pierre et Marie Curie, 75005 Paris, France*

^g*Universitat Rovira i Virgili (URV), Física i Cristal·lografia de Materials i Nanomaterials (FiCMA-FiCNA)-EMaS, Marcel·lí Domingo 1, 43007 Tarragona, Spain*

^h*Serra Hùnter Fellow*

*Corresponding author, e-mail: patrice.camy@ensicaen.fr

Abstract: A transparent “mixed” 7 at.% Er:(Lu,Sc)₂O₃ sesquioxide ceramic was fabricated by hot isostatic pressing of commercial sesquioxide powders at 1750 °C / 200 MPa in argon atmosphere. It exhibited a cubic bixbyite-type structure ($a = 10.198 \text{ \AA}$), a mean grain size of 5.7 μm and high low-signal transmission of 79.1% in the near-IR. The spectroscopic properties of Er³⁺ ions were studied. For the $^4I_{11/2} \rightarrow ^4I_{13/2}$ transition, the stimulated-emission cross-section σ_{SE} is $1.30 \times 10^{-20} \text{ cm}^2$ at 2719 nm, the corresponding luminescence branching ratio $B(JJ')$ is 19.9% and the radiative lifetime of the $^4I_{11/2}$ state is 4.80 ms, as determined using a Judd-Ofelt theory accounting for intermediate configuration interaction. The crystal-field splitting of Er³⁺ multiplets was studied at 12 K. The ceramic exhibits a significant inhomogeneous broadening of spectral bands. An Er:(Lu,Sc)₂O₃ ceramic laser generated 342 mW at 2.71 and 2.85 μm with a high slope efficiency of 41.7% (exceeding the Stokes limit) and a laser threshold of 125 mW.

Keywords: transparent ceramics; sesquioxides; erbium ion; luminescence; laser operation.

1. Introduction

The research on mid-infrared (MIR) lasers emitting around $\sim 2.8 \mu\text{m}$ is stimulated by their applications in medicine, especially in surgery [1,2]. Such radiation spectrally overlaps with the strong absorption of water vapors and liquid water; the corresponding short penetration depth in bio-tissues (few μm) enables precise incisions.

One of the most common ways to generate $\sim 2.8 \mu\text{m}$ radiation is to use erbium (Er^{3+}) doped materials according to the ${}^4I_{11/2} \rightarrow {}^4I_{13/2}$ electronic transition [3,4]. The upper laser level lifetime for this transition is typically shorter than that of the lower laser level (a self-terminating transition). Still, continuous-wave (CW) laser action at $\sim 2.8 \mu\text{m}$ can be achieved in certain Er^{3+} -doped materials due to the energy-transfer upconversion (ETU) process for adjacent ions, ${}^4I_{13/2} + {}^4I_{13/2} \rightarrow {}^4I_{15/2} + {}^4I_{11/2}$, depleting the lower laser manifold and refilling the upper one [5,6]. As a result, laser slope efficiencies exceeding the Stokes limit can be achieved owing to the energy recycling via ETU [7]. This dictates the need of high Er^{3+} doping concentrations promoting efficient ETU. Another argument for the material selection is the low phonon energy of the host matrix providing favorable ratios of upper-state to lower-state (${}^4I_{11/2}$ to ${}^4I_{13/2}$) lifetimes by reducing the multi-phonon non-radiative relaxation.

So far, cubic sesquioxides A_2O_3 (where A stands for Y, Sc, Lu or their combination) were found to be very suitable for Er^{3+} doping with the aim of $\sim 2.8 \mu\text{m}$ laser operation [8]. These crystals provide good thermal properties such as high thermal conductivity with weak concentration-dependence ($\kappa \sim 10.7 \text{ Wm}^{-1}\text{K}^{-1}$ for $\sim 7 \text{ at.}\%$ $\text{Er}:\text{Lu}_2\text{O}_3$ [9]) and positive thermo-optic coefficients [10], low phonon energies (the most intense phonon mode of Lu_2O_3 is 393 cm^{-1} [11]) and easy doping with Er^{3+} ions in high concentrations. In addition, sesquioxides provide high crystal-field strength resulting in large total Stark splitting of the ${}^4I_{13/2}$ multiplet leading to broadband emission properties [12]. Using a high-brightness pump source (an optically pumped semiconductor laser), Li *et al.* achieved an output power of 1.4 W at $\sim 2.85 \mu\text{m}$ from an $\text{Er}:\text{Lu}_2\text{O}_3$ single-crystal laser operating with a slope efficiency as high as 36% , while using a laser diode, the output was scaled up to 5.9 W at the expense of lower slope efficiency [9].

The growth of A_2O_3 single crystals is complicated because of their high melting temperatures ($2450 \text{ }^\circ\text{C}$ for Lu_2O_3). In the most developed heat exchanger growth method (HEM), the use of rhenium (Re) crucibles frequently results in uncontrolled Re impurities and coloration of crystals [13]. On the other hand, cubic sesquioxides are very suitable for the technology of transparent polycrystalline ceramics [14-16]. Their advantages include: (i) lower synthesis temperatures ($<1800 \text{ }^\circ\text{C}$, depending on the method), (ii) well-preserved spectroscopic and thermal properties, (iii) easier fabrication of solid solution compositions $(\text{A}_{1-x}\text{B}_x)_2\text{O}_3$ [17,18], (iv) well-controlled doping at high levels and (v) size-scalable production. The main challenge is reaching low optical losses and good homogeneity.

So far $\sim 2.8 \mu\text{m}$ emission from Er^{3+} sesquioxide lasers based on Lu_2O_3 [19-21] and Y_2O_3 [22-24] ceramics has been studied. Very recently, Yao *et al.* reported on a diode-pumped $\text{Er}:\text{Lu}_2\text{O}_3$ ceramic laser delivering 6.7 W at 2845 nm with a slope efficiency of 30.2% , representing record-high results in terms of output power and efficiency obtained so far [19]. Er^{3+} -doped Sc_2O_3 transparent ceramics have been also synthesized [25,26].

It is interesting to study the suitability of “mixed” sesquioxide ceramics $(\text{A}_{1-x}\text{B}_x)_2\text{O}_3$ for Er^{3+} doping with the aim of obtaining $\sim 2.8 \mu\text{m}$ laser emission. The use of solid-solution host matrix will promote inhomogeneous broadening of the spectral bands which is of interest for mode-locked lasers. Among the $(\text{A}_{1-x}\text{B}_x)_2\text{O}_3$ compositions, the system $\text{Lu}_2\text{O}_3 - \text{Sc}_2\text{O}_3$ looks attractive because of the difference in ionic radii of the host-forming cations, Lu^{3+} and Sc^{3+} , and the difference of the crystal-field strengths for these two “parent” compounds [27]. Transparent “mixed” $(\text{Lu,Sc})_2\text{O}_3$ ceramics doped with Tm^{3+} and Ho^{3+} ions for laser emission at $\sim 2 \mu\text{m}$ were studied recently [18,28]. A mode-locked $\text{Tm}:(\text{Lu,Sc})_2\text{O}_3$ ceramic laser

generated ultrashort (63 fs) pulses at 2057 nm [29] owing to the broadband gain properties of this material [18].

In the present work, we report on the synthesis, spectroscopic characterization and first $\sim 2.8 \mu\text{m}$ laser operation of a “mixed” ceramic in the $(\text{Lu},\text{Sc})_2\text{O}_3$ system doped with Er^{3+} ions.

2. Fabrication of the laser ceramics

As starting materials, we used commercial oxide powders of Er_2O_3 (purity: 99.99%), Lu_2O_3 and Sc_2O_3 (purity: 99.999%). First, they were thoroughly mixed following the formula $(\text{Er}_{0.07}\text{Lu}_{0.78}\text{Sc}_{0.15})_2\text{O}_3$. The mixture was ball milled for 24 h in ZrO_2 jars at a speed of 200 rev/min. The slurry was dried at 80°C for 24 h and the powders were sifted using a 200-mesh screen and further calcinated at a temperature of 200°C for 12 h. The green ceramic sample was dry pressed into a disk by applying a uniaxial pressure of 20 MPa, and cold isostatically pressed at 200 MPa to increase the density of the material. Before densification sintering, the samples were calcined at a temperature of 900°C for 10 h in order to remove residual carbon and organic impurities. Then, the $\text{Er}:(\text{Lu},\text{Sc})_2\text{O}_3$ disk was subjected to vacuum sintering at a temperature of 1750°C followed by hot isostatic pressing (HIPing) at 1750°C and 200 MPa in argon atmosphere for 2 h. The obtained ceramic was annealed at 1400°C for 12 h in air which removed oxygen vacancies and improved its transparency. Finally, the ceramic disk was polished from both sides.

A photograph of annealed and polished ceramic elements is shown in Fig. 1. The ceramic was transparent with rose coloration due to the Er^{3+} doping.

3. Experimental

The phase composition of the ceramic was identified by X-ray powder diffraction (XRD) using $\text{Cu K}\alpha$ radiation (1.54060 \AA) at 40 kV and 30 mA and a DX-1000CSC diffractometer (Tongda Co. Ltd). The diffractogram was measured for 2θ angles in the range from 10° to 80° with a scan speed of $1.2^\circ/\text{min}$ and a step size of 0.02. The microstructure of the polished ceramic surface was studied with a scanning electron microscope (SEM) MERLIN (Carl Zeiss). The grain size distribution was determined by direct counting method (for >100 grains) in the ImageJ software (the shape factor of 1.2 was applied).

The transmission spectrum of the ceramic was measured using a spectrophotometer (Lambda 1050, Perkin Elmer); the resolution (spectral bandwidth, SBW) was 0.25 nm in the visible and 0.7 nm in the near-IR. The luminescence spectrum at $1.4\text{--}1.8 \mu\text{m}$ was measured using an optical spectrum analyzer (AQ6375B, Yokogawa) with $\text{SBW} = 0.5 \text{ nm}$, while the measurement at $2.5\text{--}3.1 \mu\text{m}$ was performed using a 0.6 m monochromator (HRS2, Jobin-Yvon), a lock-in amplifier (SR810 DSP, Stanford Research Systems) and an InSb detector (J10D series, Judson Infrared) cooled by liquid nitrogen with $\text{SBW} = 4 \text{ nm}$. To reduce the effect of water vapor absorption, the monochromator was purged by nitrogen. The system was calibrated using a Hg lamp (Schwabe). As an excitation source, a Ti:Sapphire laser tuned to 804 nm was used.

For low-temperature (LT, 12 K) studies, the sample was mounted on an APD DE-202 closed-cycle cryo-cooler equipped with an APD HC 2 Helium vacuum cryo-compressor and a Laceshore 330 temperature controller.

The luminescence decay curves were measured using a nanosecond optical parametric oscillator (OPO, Horizon, Continuum), a $1/4 \text{ m}$ monochromator (Oriel 77200), an InGaAs detector and an 8 GHz digital oscilloscope (DSA70804B, Tektronix).

4. Characterization of the ceramics

4.1. Structural study

The phase purity of the ceramic was studied by XRD, Fig. 2. In the measured XRD pattern, only one phase was identified, namely, the cubic (sp. gr. $Ia\bar{3} - T7_h$, No. 206) sesquioxide phase with the so-called C-type or bixbyite-type structure [30] (bixbyite is a manganese iron oxide mineral with chemical formula $(Mn,Fe)_2O_3$). The diffraction peaks for the ceramic are located between those for undoped Lu_2O_3 (ICDD card #76-0162) and Sc_2O_3 (ICDD card # 84-1880). Accordingly, the lattice constant of the ceramic $a = 10.198 \text{ \AA}$, occupies an intermediate position between those of Lu_2O_3 ($a = 10.391 \text{ \AA}$) and Sc_2O_3 ($a = 9.857 \text{ \AA}$) [8]. Note that a cubic stoichiometric Er_2O_3 phase also exists ($a = 10.55 \text{ \AA}$) [31]. In the bixbyite structure, there are two rare-earth sites with the local symmetries of C_2 and C_{3i} . Both correspond to VI-fold coordination by oxygen (O^{2-}). In the sesquioxide unit-cell, there is a total of 32 cationic positions: 24 (3/4) correspond to the C_2 sites and 8 (1/4) - to the C_{3i} ones. Thus, for an ideal "parent" sesquioxide (e.g., Lu_2O_3) one may expect that the dopant ions approximately follow the same distribution. This rule is however expected to be violated in "mixed" materials due to the difference of ionic radii of the host-forming cations (Lu^{3+} (0.861 \AA) and Sc^{3+} (0.745 \AA) [32], in our case), and the dopant ions (Er^{3+} (0.890 \AA) [32], in our case). Indeed, one may expect that Er^{3+} ions will tend to replace predominantly the Lu^{3+} ones which are closer in ionic radii. The differences in the second coordination sphere of Er^{3+} ions will induce the inhomogeneous broadening of their spectral bands.

A typical SEM image of the polished surface of the $Er:(Lu,Sc)_2O_3$ ceramic is shown in Fig. 3(a). It reveals a close-packed microstructure with clean grain boundaries, a lack of secondary phases and a low concentration of μm -sized pores. The corresponding grain size distribution is shown in the inset of Fig. 3(b). The mean grain size is 5.7 μm . An environmental SEM image of a fracture surface of ceramic is presented in Fig. 3(b). It becomes evident that the intragranular fracture mechanism dominates for the ceramic.

4.2. Transmission and absorption

The transmission spectrum of the polished ceramic sample (thickness: $t = 1.0 \text{ mm}$) is shown in Fig. 4. The spectrum is dominated by absorption bands of the Er^{3+} ion. The UV absorption edge is at 0.25 μm . At a wavelength of 1.2 μm (out of Er^{3+} absorption), the measured transmission, $T = 79.1\%$ is close to the theoretical value determined by Fresnel losses and accounting for multiple reflections, $T_0 = 2n/(n^2 + 1)$, namely 82.0% (calculated assuming a linear variation of the reflective index in the $Lu_2O_3 - Sc_2O_3$ solid solution [33] yielding a value of $n = 1.916$).

The absorption coefficient was calculated as $\alpha_{\text{abs}} = -\ln(T/T_0)/t$. The absorption spectra are shown in Fig. 5. The electronic configuration of Er^{3+} is $[Xe]4f^{11}$. The observed absorption bands are due to the transitions of Er^{3+} ions from the ground-state ($^4I_{15/2}$) to excited-states from $^4I_{13/2}$ to $^4D_{7/2} + ^2D_{5/2}$. Here, the assignment is after [34]. The absorption cross-sections were calculated as $\sigma_{\text{abs}} = \alpha_{\text{abs}}/N_{\text{Er}}$, where N_{Er} is the Er^{3+} ion density ($20.0 \times 10^{20} \text{ cm}^{-3}$). It should be pointed out, that the spectroscopic properties of cubic sesquioxides are mainly determined by dopant ions residing in C_2 sites. For the C_{3i} sites, the electric dipole (ED) transitions are forbidden due to the local inversion symmetry and only magnetic dipole (MD) transitions (with $\Delta J = J - J' = 0, \pm 1$, except of $0 \leftrightarrow 0'$) are allowed. There exists an approach to calculate σ_{abs} for sesquioxides assuming (3/4) of the dopant ions are residing in the C_2 sites. As explained above, this approach is not correct for a "mixed" material, in addition, for certain Er^{3+} transitions, the MD contribution may be significant. Thus, we consider σ_{abs} as "effective" cross-section.

For the $^4I_{15/2} \rightarrow ^4I_{13/2}$ transition (which corresponds to in-band pumping for 1.6 μm lasers and terminal level pumping for $\sim 2.8 \mu\text{m}$ lasers), the maximum σ_{abs} is $1.76 \times 10^{-20} \text{ cm}^2$ at 1535 nm and the absorption bandwidth is 3.8 nm (full width at half maximum, FWHM).

For the ${}^4I_{15/2} \rightarrow {}^4I_{11/2}$ one (upper laser level pumping for $\sim 2.8 \mu\text{m}$ lasers), σ_{abs} is $0.24 \times 10^{-20} \text{ cm}^2$ at 980.6 nm.

4.3. Judd-Ofelt analysis

The transition intensities of the Er^{3+} ion in $(\text{Lu}, \text{Sc})_2\text{O}_3$ ceramic were analyzed using the Judd-Ofelt (J-O) formalism. More precisely, it was applied to ED contributions to transition intensities. The MD contributions were calculated separately within the Russell–Saunders approximation on wave functions of Er^{3+} assuming a free-ion and considering the refractive index of the host matrix. The set of reduced squared matrix elements $U^{(k)}$ in absorption and emission was calculated using the free-ion parameters from [35]. The dispersion curves for sesquioxides were taken from [33]. The details about the calculation procedure can be found elsewhere. Here, we only discuss the used approximations.

In the standard J-O theory, the ED line strengths of the $J \rightarrow J'$ transitions $S^{\text{ED}}(JJ')$ are given by [36,37]:

$$S_{\text{calc}}^{\text{ED}}(JJ') = \sum_{k=2,4,6} U^{(k)} \Omega_k, \quad (1a)$$

$$U^{(k)} = \langle (4f^n)SLJ || U^{(k)} || (4f^n)S'L'J' \rangle^2. \quad (1b)$$

Here, $U^{(k)}$ are the reduced squared matrix elements and Ω_k are the J–O parameters (or, more generally, intensity parameters). For both, $k = 2, 4$ and 6 .

For many rare-earth ions, better agreement between the experimental and calculated line strengths is achieved by accounting for configuration interaction, e.g., with the excited configuration of the opposite parity $[\text{Xe}]4f^{n-1}5d^1 = [\text{Xe}]4f^{10}5d^1$. In the case of an intermediate configuration interaction (ICI), the ED line strengths are given by [29,30]:

$$\langle S_{\text{calc}}^{\text{ED}} \rangle (JJ') = \sum_{k=2,4,6} U^{(k)} \tilde{\Omega}_k, \quad (2)$$

where $\tilde{\Omega}_k$ are the linear functions of the energies of the two multiplets (E_J and $E_{J'}$) involved in the transition:

$$\tilde{\Omega}_k = \Omega_k [1 + 2R_k (E_J + E_{J'} - 2E_f^0)], \quad (3)$$

Ω_k are new intensity parameters, R_k are the parameters representing the configuration interaction and E_f^0 is the mean energy of the $[\text{Xe}]4f^n = [\text{Xe}]4f^{11}$ configuration. In the ICI model, there are 6 free parameters, namely Ω_k and R_k ($k = 2, 4, 6$). Assuming higher-lying excited-configurations ($R_k \rightarrow 0$), leads to $\tilde{\Omega}_k = \Omega_k$ (the standard J-O theory).

In the standard J-O theory, only the excited configurations of the opposite parity are considered and it is assumed that both the $[\text{Xe}]4f^n$ configuration and the excited ones are completely degenerated. Because of this assumption, the set of Ω_k parameters is the same for all transitions. In reality, the energy gap to the excited configuration depends on the multiplet energy. Thus, the influence of excited configurations on different multiplets will not be the same, and the intensity parameters for different transitions should depend on the multiplet energies. The terms with the parameters R_k in Eq. (3) are accounting for this effect. Large values of the R_k parameters and their different signs indicate a significant influence of excited configurations with a charge transfer (covalency effects).

For the analysis, initially, 9 Er^{3+} transitions were considered (originating from the ${}^4I_{15/2}$ ground-state to the excited-states from ${}^4I_{13/2}$ to ${}^4G_{11/2}$). The experimental and calculated absorption oscillator strengths (f_{exp} and \tilde{f}_{calc} , respectively, Σ stands for the total (ED + MD) value) are listed in Table 1. The direct use of the J-O theory led to a relatively small root mean square (rms) deviation between the f_{exp} and \tilde{f}_{calc} values (0.175). However, further calculation of the radiative lifetime of the first Er^{3+} excited state, ${}^4I_{13/2}$, led to an obviously underestimated value ($\tau_{\text{rad}} = 4.75 \text{ ms}$). The use of the ICI model (the results are not shown

in Table 1) slightly improved the rms deviation (0.133) but did not solve the problem of the ${}^4I_{13/2}$ radiative lifetime ($\tau_{\text{rad}} = 4.45$ ms). This problem was recently discussed by Merkle *et al.* for Er:Lu₂O₃ [31]. The authors concluded that it arises from a significant contribution of Er³⁺ ions located in C_{3i} sites to MD allowed transition ${}^4I_{15/2} \rightarrow {}^4I_{13/2}$.

To overcome this problem, we excluded the ${}^4I_{15/2} \rightarrow {}^4I_{13/2}$ transition in absorption from the fit (a total of 8 transitions was thus analyzed). In this case, a reasonable $\tau_{\text{rad}}({}^4I_{13/2})$ value was obtained for both the J-O and ICI theories. The latter model was selected for further calculations for two reasons: first, it provided smaller rms deviation (0.038) and second, much better agreement between f_{exp} and f_{calc} for another transition of interest, ${}^4I_{15/2} \rightarrow {}^4I_{11/2}$, as compared to the standard J-O one.

The obtained intensity parameters are listed in Table 2. For the ICI theory (when excluding the ${}^4I_{15/2} \rightarrow {}^4I_{13/2}$ transition from the fit), they are $\Omega_2 = 7.267$, $\Omega_4 = 1.784$ and $\Omega_6 = 0.664 [10^{-20} \text{ cm}^2]$ and $R_2 = -0.012$, $R_4 = -0.084$ and $R_6 = 0.168 [10^{-4} \text{ cm}]$.

Based on these intensity parameters, the probabilities of spontaneous radiative transitions $A_{\text{calc}}^{\Sigma}(\text{JJ}')$, the luminescence branching ratios $B(\text{JJ}')$ and the radiative lifetimes of the excited-states τ_{rad} were calculated for the excited-states from ${}^4I_{13/2}$ up to ${}^4S_{3/2} + {}^2H_{11/2}$ (considering the latter two states as thermally coupled ones), Table 3. For the first excited state (${}^4I_{13/2}$), $\tau_{\text{rad}} = 6.28$ ms and for the ${}^4I_{11/2}$ one, $\tau_{\text{rad}} = 4.80$ ms. The luminescence branching ratio for the ${}^4I_{11/2} \rightarrow {}^4I_{13/2}$ transition which gives rise to laser emission at $\sim 2.8 \mu\text{m}$, $B(\text{JJ}') = 19.9\%$.

4.4. Emission (spectra and lifetime)

Two transitions in emission, ${}^4I_{13/2} \rightarrow {}^4I_{15/2}$ (at $\sim 1.6 \mu\text{m}$) and ${}^4I_{11/2} \rightarrow {}^4I_{13/2}$ (at $\sim 2.8 \mu\text{m}$) were analyzed. For both, the stimulated-emission (SE) cross-sections, σ_{SE} , were calculated using the Füchtbauer–Ladenburg (F-L) formula [32]:

$$\sigma_{\text{SE}}(\lambda) = \frac{\lambda^5}{8\pi \langle n \rangle^2 \tau_{\text{rad}} c} \frac{B(\text{JJ}')W'(\lambda)}{\int \lambda W'(\lambda) d\lambda}, \quad (4)$$

where, λ is the light wavelength, $\langle n \rangle$ is the refractive index of the ceramic corresponding to the mean luminescence wavelength $\langle \lambda_{\text{lum}} \rangle$, τ_{rad} corresponds to the emitting state (${}^4I_{13/2}$ or ${}^4I_{11/2}$) and $B(\text{JJ}')$ – to the considered transition, c is the speed of light and $W(\lambda)$ is the luminescence spectrum accounting for the apparatus function of the set-up. For the ${}^4I_{13/2} \rightarrow {}^4I_{15/2}$ transition for which reabsorption is expected to be particularly strong in highly doped ceramic, a complementary approach was also used, i.e., the reciprocity method (RM) [33]:

$$\sigma_{\text{SE}}(\lambda) = \sigma_{\text{abs}}(\lambda) \frac{Z_1}{Z_2} \exp\left(-\frac{(hc/\lambda) - E_{\text{ZPL}}}{kT}\right), \quad (5a)$$

$$Z_m = \sum_k g_k^m \exp(-E_k^m / kT). \quad (5b)$$

Here, h is the Planck constant, k is the Boltzmann constant, T is the temperature (RT), E_{ZPL} is the energy corresponding to the so-called zero-phonon-line (ZPL) transition occurring between the lowest Stark sub-levels of the involved multiplets, Z_m are the so-called partition functions of the lower ($m = 1$) and upper ($m = 2$) manifolds, and $g_k^m = 1$ is the degeneracy of the Stark sub-level with a number k and energy E_k^m measured from the lowest sub-level of each multiplet. The data on the crystal-field splitting for Er³⁺ obtained in the present work were used (Section 4.5).

For the ${}^4I_{13/2} \rightarrow {}^4I_{15/2}$ transition, the simultaneous use of the F-L equation and RM gives a good agreement at wavelength above $1.6 \mu\text{m}$ (where the reabsorption becomes weak) for the $\tau_{\text{rad}}({}^4I_{13/2})$ values of 8.0 ± 0.5 ms which reasonably agrees with the J-O analysis, Fig. 6(a). The maximum σ_{SE} is $1.43 \times 10^{-20} \text{ cm}^2$ at 1535 nm (corresponding to ZPL at RT)

and at longer wavelengths where the laser operation is expected, σ_{SE} is lower, namely $0.14 \times 10^{-20} \text{ cm}^2$ at 1658 nm, Fig. 6(a).

For the $^4I_{11/2} \rightarrow ^4I_{13/2}$ transition, the SE cross-sections determined using the F-L equation are $1.30 \times 10^{-20} \text{ cm}^2$ at 2718 nm (ZPL) and $0.35 \times 10^{-20} \text{ cm}^2$ at 2859 nm, Fig. 6(b). The corresponding emission bandwidths (FWHM) are 25 and 44 nm, respectively.

Using the reciprocity method, Eq. (5), we have also calculated the spectrum of excited-state absorption (ESA) corresponding to the $^4I_{13/2} \rightarrow ^4I_{11/2}$ transition, Fig. 6(b).

The RT luminescence decay curves from the $^4I_{13/2}$ and $^4I_{11/2}$ states of Er^{3+} ions in 7 at.% $\text{Er}:(\text{Lu},\text{Sc})_2\text{O}_3$ ceramics, plotted in a semi-log scale are shown in Fig. 7. Both of them are measured under resonant excitation using small quantities of finely powdered ceramic to reduce the effect of radiation trapping (reabsorption).

The decay curve from the $^4I_{13/2}$ state, Fig. 7(a), is not single-exponential while it is well fitted using the Inokuti-Hirayama (I-H) model accounting for the energy transfer processes in the absence of migration [34]:

$$I(t) = I_0 \exp\left(-\frac{t}{\tau_0} - \alpha \left(\frac{t}{\tau_0}\right)^{3/s}\right), \quad (6)$$

where, $I(t)$ is the emission intensity after pulsed excitation, τ_0 is the lifetime of an isolated donor (D) or the so-called intrinsic lifetime, the parameter s stands for the mechanism of the ion interaction ($s = 6$ and $s = 8$ for dipole-dipole (D-D) and dipole-quadrupole (D-Q) processes, respectively) and α is a constant describing the probability of energy-transfer. For the curve shown in Fig. 7(a), the best-fit parameters are $\tau_0 = 11.7 \pm 0.3 \text{ ms}$, $s = 7.0 \pm 0.1$ (predominantly D-D interaction) and $\alpha = 2.15 \pm 0.1$.

The luminescence decay curve from the $^4I_{11/2}$ state strongly deviates from a single-exponential law. The attempt to use the I-H model for its description failed. The observation of a nearly single-exponential “fast” decay component, as well as another “slow” component at longer times suggested the presence of two ion classes. As mentioned above, the Er^{3+} ions in the ceramic may reside in C_2 and C_{3i} sites. However, the $^4I_{11/2} \rightarrow ^4I_{15/2}$ transition is of purely ED nature and it cannot reveal the signatures of the C_{3i} sites. Thus, we assume that the observed difference in lifetime for the two ion classes may arise from strong energy-migration (among the active ions and to defects and uncontrolled impurities). The model of migration-assisted energy-transfer is [35]:

$$I(t) = I_0 \exp\left(-\frac{t}{\tau_0} - \omega t - \alpha \left(\frac{t}{\tau_0}\right)^{3/s}\right), \quad (7)$$

where ω is the energy-migration rate expressed in s^{-1} . We assume that ions belonging to class #1 experience ETU and weak EM ($\omega \approx 0$) and ions belonging to class #2 – ETU and strong EM leading to effective shortening of their intrinsic lifetime, $1/\tau_0^* = (1/\tau_0) - \omega$. For the decay curve shown in Fig. 7(b), the best-fit parameters are $\tau_0 = 4.6 \pm 0.2 \text{ ms}$, $s = 6.1 \pm 0.1$ (D-D interaction), $\alpha = 2.86 \pm 0.1$ (class #1) and $\tau_0^* = 0.60 \pm 0.1 \text{ ms}$, or, equivalently, $\omega = 1.45 \times 10^3 \text{ s}^{-1}$ (class #2). Note that due to the strong EM, it is not possible to quantify precisely the α value in the latter case.

The appearance of different ion classes in polycrystalline ceramics is not surprising. The granular structure of ceramics determines variation of compositional and crystallographic properties at the level of each particular grain. One can suggest two possible mechanisms of formation of two spectroscopically distinct ion classes in “mixed” ceramics. The first is the possible segregation of dopant ions at the grain boundaries where the interaction between the ions themselves and with defect and impurity centers is greatly promoted. It was indeed observed using high-resolution transmission electron microscopy in sesquioxide ceramics [36]. However, the authors of [36] concluded that it is relatively weak for small cations located in the end of the lanthanide series (as in the case of Er^{3+} replacing Lu^{3+}). Thus, this effect is expected to be hardly visible at the level of macroscopic spectroscopic properties. Second, as pointed out above, one may expect a predominant

substitution of Lu³⁺ by Er³⁺ leading to depletion of these host-forming cations in other regions. Thus, locally, two types of centers differing by the second coordination sphere composed mainly by Lu³⁺ or Sc³⁺ can be formed. It was found that among the A₂O₃ family materials, particularly for Sc₂O₃, the luminescence lifetime of the ⁴I_{11/2} Er³⁺ state is notably shortened (τ_{lum} is about 0.34-0.55 ms [37,38] even at low doping levels) as compared to its Lu₂O₃ and Y₂O₃ counterparts for which τ_{lum} is about ~2 ms at RT and 4.5 ms at LT. This matches well our observations.

For both luminescence decay curves, the mean decay time was also calculated as:

$$\langle \tau_{lum} \rangle = \frac{\int t \cdot I(t) dt}{\int I(t) dt}. \quad (8)$$

For the decay from the ⁴I_{13/2} and ⁴I_{11/2} multiplets, $\langle \tau_{lum} \rangle$ amounted to 4.89 and 1.07 ms, respectively. These values agree well with the previously reported data for single-crystals of Er:Lu₂O₃ [9].

4.5. Low-temperature spectroscopy

The expected inhomogeneous broadening of spectral bands of Er³⁺ ions in the “mixed” ceramic is revealed at low temperature. The LT (12 K) absorption and luminescence spectra used to determine the crystal-field splitting of Er³⁺ multiplets involved in the near- and mid-IR emissions (from ⁴I_{15/2} to ⁴I_{11/2}) are shown in Fig. 8.

For Er³⁺ ions in C₂ sites, each ^{2S+1}L_J multiplet splits into J + 1/2 non-degenerated Stark sub-levels (considering non-integer J). Following the early work by Dieke [39], we will use empirical notations for these sub-levels, namely Z_i (i = 1...8), Y_j (j = 1...7) and A_k (k = 1...6) for the ⁴I_{15/2}, ⁴I_{13/2} and ⁴I_{11/2} multiplets, respectively [40]. To simplify the assignment of electronic transitions, we used the crystal-field data for Er³⁺ ions in Sc₂O₃ derived by Lupei *et al.* [38] (shown by vertical dashes in Fig. 8). The bands related to electronic transitions of Er³⁺ ions in C₂ sites in the (Lu,Sc)₂O₃ ceramic experience a significant inhomogeneous broadening, as compared to Er³⁺-doped “parent” sesquioxides [37,40].

We have determined experimentally the Stark energies for all Er³⁺ multiplets from ⁴I_{15/2} up to ⁴G_{11/2} (except of few missing levels), Table 4. The corresponding energy-level scheme is shown in Fig. 9(a) together with the processes relevant for ~2.8 μm laser operation. A close look on the crystal-field splitting of the ⁴I_{11/2} and ⁴I_{13/2} multiplets is given in Fig. 9(b).

As pointed out above, the spectroscopic signatures of Er³⁺ ions in C_{3i} sites can be found for the MD ⁴I_{15/2} → ⁴I_{13/2} transition. In the present work, the intense and narrow peak at 6539 cm⁻¹ is unambiguously assigned to C_{3i} sites in agreement with the findings of Gruber *et al.* for Er:Y₂O₃ [41]. Other possible peaks are hardly resolved because of the broad bands due to the C₂ site absorption.

5. Laser operation

5.1. Laser set-up

The scheme of the laser set-up is shown in Fig. 10. A rectangular active element (thickness: 1.98 mm, aperture: 3.0×3.0 mm²) was fabricated from the 7 at.% Er:(Lu,Sc)₂O₃ ceramic. It was polished to laser-grade quality from both sides and remained uncoated. The element was mounted on a passively cooled Cu-holder using a heat-conductive silver paint. A hemispherical cavity consisted of a flat pump mirror (PM) coated for high transmission (HT) at 0.78-0.83 and 0.92-1.06 μm (the pump ranges) and for high reflection (HR) at 2.6-3.0 μm and a concave output coupler (OC) with a radius of curvature (RoC) of -75 mm and a transmission $T_{OC} = 1.5 \pm 0.5\%$ at 2.6-3.0 μm. The geometrical cavity length was ~75 mm. The laser element was placed close to the PM with an air gap of less than 1 mm.

As a pump source, we used a CW Ti:Sapphire laser (model 3900S, Spectra Physics) operating in the fundamental mode (TEM₀₀, M² ≈ 1) and delivering up to 2.7 W at 804.4 nm and 2.15 W at 980.6 nm. The pump radiation was focused into the laser element through the PM using an achromatic lens (f = 75 mm). The OC was partially reflective for the pump (i.e., the pumping was in double pass). The total pump absorption under lasing conditions $\eta_{\text{abs,L}}$ amounted to 60.2% and 47.1% for $\lambda_P = 804.4$ and 980.6 nm, respectively.

The spectra of laser emission were detected using a Fourier transform laser spectrum analyzer (771 series, Bristol). The laser mode was captured using a pyroelectric camera (Pyrocam IIIHR, Ophir-Spiricon).

5.2. Laser performance

Two pump schemes were employed, namely, pumping into the ⁴I_{11/2} and ⁴I_{9/2} Er³⁺ multiplets, Fig. 11. For optimum $\lambda_P = 980.6$ nm, the laser generated a maximum output power of 342 mW at ~2717 and 2853-2864 nm with a slope efficiency η of 41.7% (with respect to the absorbed pump power) and a laser threshold P_{th} of 125 mW. The optical-to-optical efficiency η_{opt} amounted to 16.5% (versus the power incident on the ceramic). Power scaling was limited by the available pump. Almost no signs of thermal effects were observed in the input-output dependence. The η value exceeded the Stokes efficiency under lasing conditions, $\eta_{\text{St,L}} = \lambda_P/\lambda_L \approx 34\%$, indicating an efficient ETU process (#1), Fig. 9(a), refilling the population of the upper laser manifold.

For pumping into the ⁴I_{9/2} state ($\lambda_P = 804.4$ nm), the laser output reached 254 mW at ~2717 and 2853 nm with lower slope efficiency of 23.7% and nearly the same threshold, 142 mW. For absorbed pump powers exceeding 1.1 W, a thermal roll-over was observed. It is related to stronger heat loading for this pump scheme (in particular, the energy loss related to multiphonon non-radiative relaxation between the ⁴I_{9/2} and ⁴I_{11/2} states).

Typical spectra of laser emission are shown in Fig. 11(b). Lasing in two spectral regions, at ~2.71 and 2.85 μm , was observed. For the latter we consider two possible reasons. First, the main peak in the SE cross-section spectrum for the ⁴I_{11/2} → ⁴I_{13/2} transition overlaps with the structured water vapor absorption in the atmosphere, Fig. 6(b), which may introduce additional loss. Second, a resonant excited-state absorption (ESA) process, ⁴I_{13/2} → ⁴I_{11/2}, which becomes efficient at high populations of the metastable ⁴I_{13/2} state, forces the laser to operate at wavelengths longer than the ZPL (~2.71 μm).

The laser operated in the fundamental transverse mode, see the mode profile in the inset of Fig. 11(b).

For both studied pump schemes, the laser excitation curves (i.e., the dependence of the output power on the pump wavelength at a fixed incident pump power) were measured. They are shown in Fig. 12 together with the absorption cross-section spectra for the ⁴I_{15/2} → ⁴I_{11/2} and ⁴I_{9/2} Er³⁺ transitions. The laser excitation curves follow the shape of the σ_{abs} spectra indicating that pumping into the most intense absorption peak is preferable for relatively short samples. CW laser operation was achieved for λ_P in the ranges of 957-1001 nm and 786-820 nm, limited by the weak pump absorption and coatings of the laser mirrors.

6. Conclusions

To conclude, we report on the fabrication of high optical quality 7 at.% Er:(Lu,Sc)₂O₃ single-phase (C-type structure) transparent sesquioxide ceramic, its detailed spectroscopic study and first laser operation. The ceramic is fabricated by vacuum sintering at 1750 °C followed by HIPing at 1750 °C / 200 MPa using high-purity commercial sesquioxide powders. It exhibits close-packed microstructure (mean grain size: 5.7 μm), as well as high transmission in the near-IR, close to the theoretical one. The compositional disorder of the host matrix promoted by a great difference of ionic radii of the host-forming cations (Lu³⁺

and Sc^{3+}) leads to a significant inhomogeneous broadening of the absorption and emission bands revealed at 12 K. At RT, the “mixed” ceramic features broadband mid-IR emission properties, i.e., an emission bandwidth exceeding 40 nm around $\sim 2.86 \mu\text{m}$. The high Er^{3+} doping level results in favorable upper-level to lower-level lifetime ratio for the $^4I_{11/2} \rightarrow ^4I_{13/2}$ transition ($\langle \tau_{\text{lum}} \rangle = 1.07 \text{ ms}$ and 4.89 ms , respectively).

Continuous-wave mid-infrared laser operation of the 7 at.% $\text{Er}:(\text{Lu},\text{Sc})_2\text{O}_3$ ceramic is demonstrated under pumping into the $^4I_{11/2}$ state (at $\sim 0.98 \mu\text{m}$) and the $^4I_{9/2}$ one (at $\sim 0.8 \mu\text{m}$). In the former case, the ceramic laser generated 342 mW at 2.71 and 2.85 μm with a slope efficiency of 41.7% (a record-high value for Er sesquioxide ceramic lasers) and a low laser threshold of only 125 mW. The observed slope efficiency exceeds the Stokes limit indicating an efficient ETU process recycling the population of the upper laser manifold.

Acknowledgements

This work was supported by Spanish Government, Ministry of Science and Innovation (project No. PID2019-108543RB-I00) and by Generalitat de Catalunya (project No. 2017SGR755). Wei Jing acknowledges financial support from the National Natural Science Foundation of China (grant No. 61805219) and the Key Laboratory of Science and Technology on High Energy Laser, CAEP.

References

1. T. Harashima, J.I. Kinoshita, Y. Kimura, A. Brugnera, F. Zanin, J.D. Pecora, K. Matsumoto, Morphological comparative study on ablation of dental hard tissues at cavity preparation by Er:YAG and Er,Cr:YSGG lasers, *Photomed. Laser Surg.* 23(1) (2005) 52-55.
2. S. Stübinger, Advances in bone surgery: the Er:YAG laser in oral surgery and implant dentistry, *Clin. Cosmet. Investig. Dent.* 2 (2010) 47-62.
3. R.C. Stoneman, L. Esterowitz, Efficient resonantly pumped 2.8- μm Er^{3+} :GSGG laser, *Opt. Lett.* 17 (1992) 816-818.
4. T. Jensen, A. Dening, G. Huber, B.H.T. Chai, Investigation of diode-pumped 2.8- μm $\text{Er}:\text{LiYF}_4$ lasers with various doping levels, *Opt. Lett.* 21 (1996) 585-587.
5. M. Pollnau, W. Lüthy, H.P. Weber, T. Jensen, G. Huber, A. Cassanho, H.P. Jenssen, R.A. McFarlane, Investigation of diode-pumped 2.8- μm laser performance in $\text{Er}:\text{BaY}_2\text{F}_8$, *Opt. Lett.* 21 (1996) 48-50.
6. M. Pollnau, T. Graf, J.E. Balmer, W. Lüthy, H.P. Weber, Explanation of the cw operation of the Er^{3+} 3- μm crystal laser, *Phys. Rev. A.* 49 (1994) 3990-3996.
7. M. Pollnau, R. Spring, C. Ghisler, S. Wittwer, W. Luthy, and H.P. Weber, Efficiency of erbium 3- μm crystal and fiber lasers, *IEEE J. Quantum Electron.* 32 (1996) 657-663.
8. C. Kränkel, Rare-earth-doped sesquioxides for diode-pumped high-power lasers in the 1-, 2-, and 3- μm spectral range, *IEEE J. Sel. Top. Quantum Electron.* 21 (2014) 250-262.
9. T. Li, K. Beil, C. Kränkel, G. Huber, Efficient high-power continuous wave $\text{Er}:\text{Lu}_2\text{O}_3$ laser at 2.85 μm , *Opt. Lett.* 37 (2012) 2568-2570.
10. P.A. Loiko, K.V. Yumashev, R. Schödel, M. Peltz, C. Liebald, X. Mateos, B. Deppe, and C. Kränkel, Thermo-optic properties of $\text{Yb}:\text{Lu}_2\text{O}_3$ single crystals, *Appl. Phys. B* 120 (2015) 601-607.
11. L. Laversenne, Y. Guyot, C. Goutaudier, M.T. Cohen-Adad, and G. Boulon, Optimization of spectroscopic properties of Yb^{3+} -doped refractory sesquioxides: cubic Y_2O_3 , Lu_2O_3 and monoclinic Gd_2O_3 , *Opt. Mater.* 16 (2001) 475-483.
12. I. Trabelsi, R. Maâlej, M. Dammak, A. Lupei, M. Kamoun, Crystal field analysis of Er^{3+} in Sc_2O_3 transparent ceramics, *J. Lumin.* 130 (2010) 927-931.
13. R. Peters, C. Kränkel, K. Petermann, G. Huber, Crystal growth by the heat exchanger method, spectroscopic characterization and laser operation of high-purity $\text{Yb}:\text{Lu}_2\text{O}_3$, *J. Cryst. Growth.* 310 (2008) 1934-1938.
14. J. Lu, K. Takaichi, T. Uematsu, A. Shirakawa, M. Musha, K.I. Ueda, H. Yagi, T. Yanagitani, A.A. Kaminskii, $\text{Yb}^{3+}:\text{Y}_2\text{O}_3$ ceramics—a novel solid-state laser material, *Jpn. J. Appl. Phys.* 41 (2002) L1373-L1375.

15. K. Takaichi, H. Yagi, A. Shirakawa, K. Ueda, S. Hosokawa, T. Yanagitani, A.A. Kaminskii, Lu₂O₃:Yb³⁺ ceramics—a novel gain material for high-power solid-state lasers, *Phys. Status Solidi A*. 202 (2005) R1-R3.
16. J. Lu, J. F. Bisson, K. Takaichi, T. Uematsu, A. Shirakawa, M. Musha, K. Ueda, H. Yagi, T. Yanagitani, A. A. Kaminskii, Yb³⁺:Sc₂O₃ ceramic laser, *Appl. Phys. Lett.* 83 (2003) 1101-1103.
17. G. Toci, A. Pirri, B. Patrizi, R.N. Maksimov, V.V. Osipov, V.A. Shitov, M. Vannini, Yb³⁺:(Lu_xY_{1-x})₂O₃ mixed sesquioxide ceramics for laser applications. Part II: Laser performances, *J. Alloys Compd.* 853 (2021) 156943-1-8.
18. W. Jing, P. Loiko, J.M. Serres, Y. Wang, E. Vilejshikova, M. Aguiló, F. Díaz, U. Griebner, H. Huang, V. Petrov, X. Mateos, Synthesis, spectroscopy, and efficient laser operation of “mixed” sesquioxide Tm:(Lu,Sc)₂O₃ transparent ceramics, *Opt. Mater. Express* 7 (2017) 4192-4202.
19. W. Yao, H. Uehara, S. Tokita, H. Chen, D. Konishi, M. Murakami, R. Yasuhara, LD-pumped 2.8 μm Er:Lu₂O₃ ceramic laser with 6.7 W output power and > 30% slope efficiency, *Appl. Phys. Express.* 14 (2020) 012001-1-4.
20. H. Uehara, S. Tokita, J. Kawanaka, D. Konishi, M. Murakami, S. Shimizu, R. Yasuhara, Optimization of laser emission at 2.8 μm by Er:Lu₂O₃ ceramics, *Opt. Express* 26 (2018) 3497-3507.
21. H. Uehara, R. Yasuhara, S. Tokita, J. Kawanaka, M. Murakami, S. Shimizu, Efficient continuous wave and quasi-continuous wave operation of a 2.8 μm Er:Lu₂O₃ ceramic laser, *Opt. Express* 25 (2017) 18677-18684.
22. L. Wang, H. Huang, D. Shen, J. Zhang, H. Chen, D. Tang, Diode-pumped high power 2.7 μm Er:Y₂O₃ ceramic laser at room temperature, *Opt. Mater.* 71 (2017) 70-73.
23. J. Mužík, R. Yasuhara, M. Smrž, V. Kubeček, T. Mocek, A high-brightness room temperature 2.7 μm Er:Y₂O₃ ceramic laser, *Laser Phys. Lett.* 16 (2019) 0358011-1-5.
24. T. Sanamyan, J. Simmons, M. Dubinskii, Er³⁺-doped Y₂O₃ ceramic laser at ~ 2.7 μm with direct diode pumping of the upper laser level, *Laser Phys. Lett.* 7 (2010) 206-209.
25. C. Gheorghie, S. Georgescu, V. Lupei, A. Lupei, A. Ikesue, Absorption intensities and emission cross section of Er³⁺ in Sc₂O₃ transparent ceramics, *J. Appl. Phys.* 103 (2008) 083116-1-5.
26. K. Serivalsatit, J. Ballato, Submicrometer grain-sized transparent erbium-doped scandia ceramics, *J. Am. Ceram. Soc.* 93 (2010) 3657-3662.
27. P. Loiko, P. Koopmann, X. Mateos, J.M. Serres, V. Jambunathan, A. Lucianetti, T. Mocek, M. Aguiló, F. Diaz, U. Griebner, V. Petrov, Highly efficient, compact Tm³⁺:RE₂O₃ (RE= Y, Lu, Sc) sesquioxide lasers based on thermal guiding, *IEEE J. Sel. Top. Quantum Electron.* 24 (2018) 1600713-1-13.
28. W. Jing, P. Loiko, J.M. Serres, Y. Wang, E. Kifle, E. Vilejshikova, M. Aguiló, F. Díaz, U. Griebner, H. Huang, V. Petrov, Synthesis, spectroscopic characterization and laser operation of Ho³⁺ in “mixed” (Lu,Sc)₂O₃ ceramics, *J. Lumin.* 203 (2018) 145-151.
29. Y. Wang, W. Jing, P. Loiko, Y. Zhao, H. Huang, X. Mateos, S. Suomalainen, A. Härkönen, M. Guina, U. Griebner, V. Petrov, Sub-10 optical-cycle passively mode-locked Tm:(Lu_{2/3}Sc_{1/3})₂O₃ ceramic laser at 2 μm, *Opt. Express* 26 (2018) 10299-10304.
30. M. Guzik, J. Pejchal, A. Yoshikawa, A. Ito, T. Goto, M. Siczek, T. Lis, G. Boulon, Structural investigations of Lu₂O₃ as single crystal and polycrystalline transparent ceramic, *Cryst. Growth Des.* 14 (2014) 3327-3334.
31. Q. Guo, Y. Zhao, C. Jiang, W.L. Mao, Z. Wang, J. Zhang, Y. Wang, Pressure-induced cubic to monoclinic phase transformation in erbium sesquioxide Er₂O₃, *Inorg. Chem.* 46 (2007) 6164-6169.
32. R.D. Shannon, Revised effective ionic radii and systematic studies of interatomic distances in halides and chalcogenides, *Acta Cryst. A*. 32 (1976) 751-767.
33. D.E. Zelmon, J.M. Northridge, N.D. Haynes, D. Perlov, K. Petermann, Temperature-dependent Sellmeier equations for rare-earth sesquioxides, *Appl. Opt.* 52 (2013) 3824-3828.
34. W.T. Carnall, P.R. Fields, K. Rajnak, Electronic energy levels in the trivalent lanthanide aquo ions. I. Pr³⁺, Nd³⁺, Pm³⁺, Sm³⁺, Dy³⁺, Ho³⁺, Er³⁺, and Tm³⁺, *J. Chem. Phys.* 49 (1968) 4424-4442.
35. J. B. Gruber, J. R. Quagliano, M. F. Reid, F. S. Richardson, M. F. Hills, V. D. Seltzer, S. B. Stevens, C. A. Morrison, T. H. Alik, Energy levels and correlation crystal-field effects in Er³⁺-doped garnets, *Phys. Rev. B* 48 (1993) 15561-15573.
36. B. R. Judd, Optical absorption intensities of rare-earth ions, *Phys. Rev.* 127 (1962) 750-761.
37. G. S. Ofelt, Intensities of crystal spectra of rare-earth ions, *J. Chem. Phys.* 37 (1962) 511-520.

29. A.A. Kornienko, A.A. Kaminskii, E.B. Dunina, Dependence of the line strength of f–f transitions on the manifold energy. II. Analysis of Pr³⁺ in KPrP₄O₁₂, Phys. Status Solidi B 157 (1990) 267-273.
30. P. Loiko, A. Volokitina, X. Mateos, E. Dunina, A. Kornienko, E. Vilejshikova, M. Aguilo, F. Diaz, Spectroscopy of Tb³⁺ ions in monoclinic KLu(WO₄)₂ crystal: application of an intermediate configuration interaction theory, Opt. Mater. 78 (2018) 495-501.
31. L.D. Merkle, N. Ter-Gabrielyan, N.J. Kacik, T. Sanamyan, H. Zhang, H. Yu, J. Wang, M. Dubinskii, Er:Lu₂O₃ – Laser-related spectroscopy, Opt. Mater. Express 3 (2013) 1992-2002.
32. B. Aull, H. Jenssen, Vibronic interactions in Nd:YAG resulting in nonreciprocity of absorption and stimulated emission cross sections, IEEE J. Quantum Electron. 18 (1982) 925-930.
33. S. A. Payne, L. L. Chase, L. K. Smith, W. L. Kway, W. F. Krupke, Infrared cross-section measurements for crystals doped with Er³⁺, Tm³⁺ and Ho³⁺, IEEE J. Quantum Electron. 28 (1992) 2619-2630.
34. M. Inokuti, F. Hirayama, Influence of energy transfer by the exchange mechanism on donor luminescence, J. Chem. Phys. 43 (1965) 1978-1989.
35. A.I. Burshtein, Hopping mechanism of energy transfer, Sov. Phys. JETP 35 (1972) 882-885.
36. T. Epicier, G. Boulon, W. Zhao, M. Guzik, B. Jiang, A. Ikesue, L. Esposito, Spatial distribution of the Yb³⁺ rare earth ions in Y₃Al₅O₁₂ and Y₂O₃ optical ceramics as analyzed by TEM, J. Mater. Chem. 22 (2012) 18221-18229.
37. A. Lupei, V. Lupei, C. Gheorghe, A. Ikesue, Excited states dynamics of Er³⁺ in Sc₂O₃ ceramic, J. Lumin. 128 (2008) 918-920.
38. T. Sanamyan, J. Simmons, M. Dubinskii, Efficient cryo-cooled 2.7-μm Er³⁺:Y₂O₃ ceramic laser with direct diode pumping of the upper laser level, Laser Phys. Lett. 7 (2010) 569-572.
39. F. Varsanyi, G.H. Dieke, Energy levels of hexagonal ErCl₃, J. Chem. Phys. 36 (1962) 2951-2961.
40. P. Kisliuk, W.F. Krupke, J.B. Gruber, Spectrum of Er³⁺ in single crystals of Y₂O₃, J. Chem. Phys. 40 (1964) 3606-3610.
41. J.B. Gruber, R.P. Leavitt, C.A. Morrison, N.C. Chang, Optical spectra, energy levels, and crystal-field analysis of tripositive rare-earth ions in Y₂O₃. IV. C_{3i} sites, J. Chem. Phys. 82 (1985) 5373-5378.

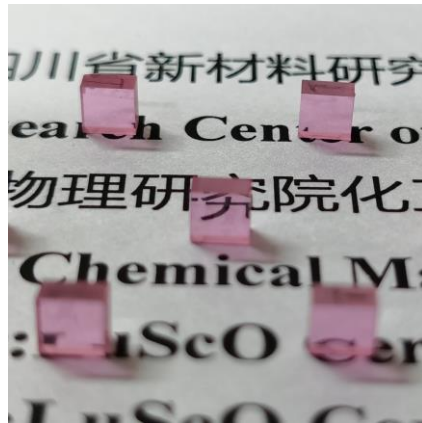


Fig. 1. Photograph of annealed and polished Er:(Lu,Sc)₂O₃ ceramic elements.

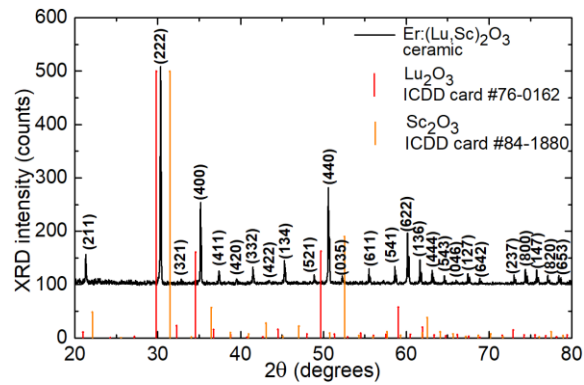


Fig. 2. X-ray powder diffraction pattern of Er:(Lu,Sc)₂O₃ ceramic, *red and orange peaks* – theoretical patterns for Lu₂O₃ (ICDD card #76-0162) and Sc₂O₃ (ICDD card #84-1880), respectively, *numbers* – Miller's indices (*hkl*).

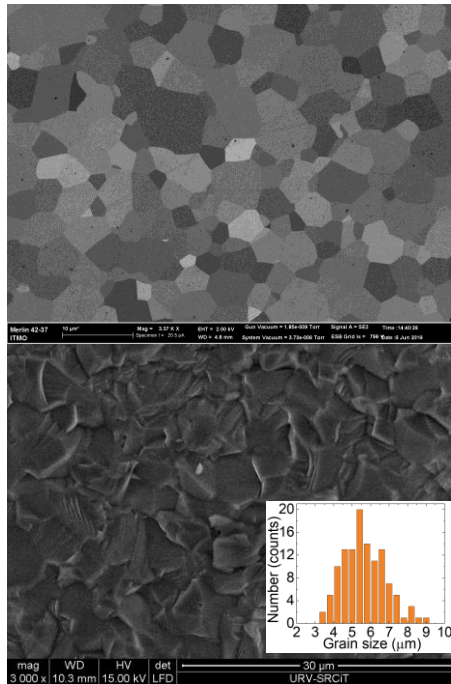


Fig. 3. Microstructure of Er:(Lu,Sc)₂O₃ ceramic: (a) SEM images of the polished surface; (b) environmental SEM image of the fracture surface. Inset in (b) – grain size distribution. Scale

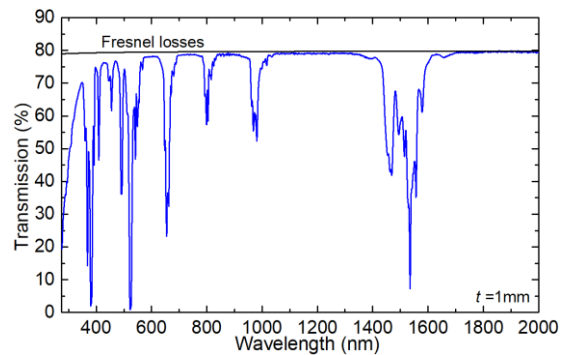


Fig. 4. Transmission spectrum of a laser-grade-polished Er:(Lu,Sc)₂O₃ ceramic disk (thickness, $t = 1.0$ mm), black curve – theoretical transmission determined by the Fresnel losses.

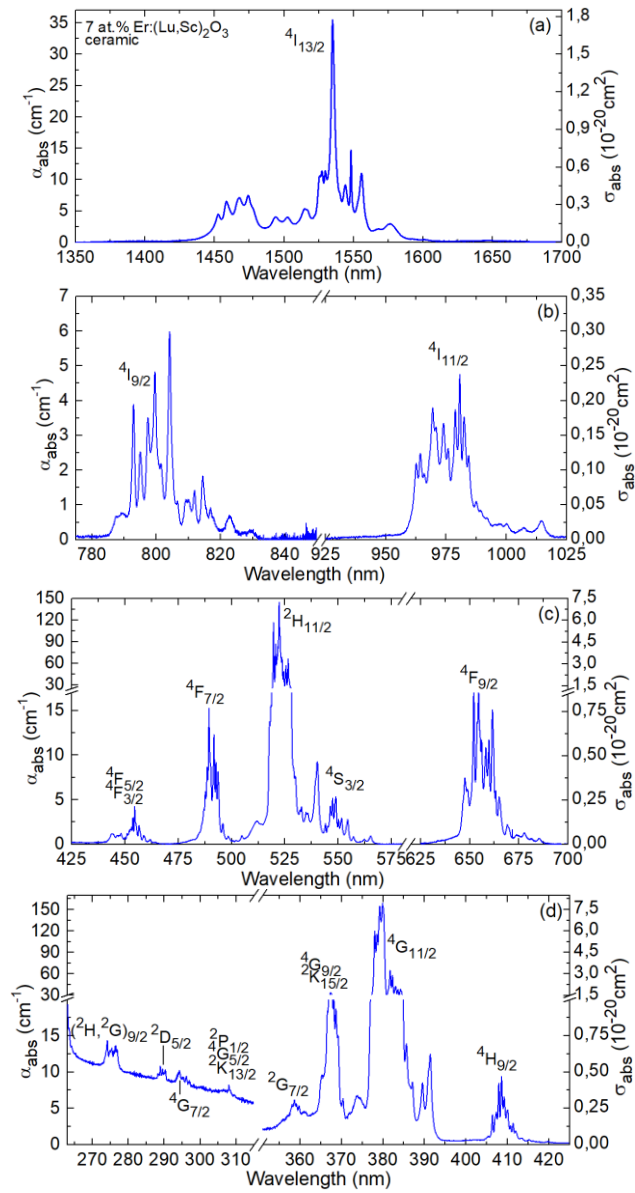


Fig. 5. (a-d) RT absorption spectra of 7 at.% Er:(Lu,Sc)₂O₃ ceramic (α_{abs} – absorption coefficient, $\sigma_{\text{abs}} = \alpha_{\text{abs}}/N_{\text{Er}}$ – absorption cross-section).

Table 1. Analysis of transition intensities* in absorption for Er³⁺ ions in (Lu,Sc)₂O₃ ceramic.

Transition ⁴ I _{15/2} → ² S+ ¹ L _J	$\langle E \rangle$, cm ⁻¹	Γ , cm ⁻¹ *nm	f_{exp} , 10 ⁻⁶	f_{calc} , 10 ⁻⁶		
				J-O	J-O**	ICI**
⁴ I _{13/2}	6558	819.85	2.020	1.191 ^{ED} + 0.592 ^{MD}	0.930 ^{ED} + 0.592 ^{MD}	0.757 ^{ED} + 0.592 ^{MD}
⁴ I _{11/2}	10145	82.62	0.489	0.652 ^{ED}	0.524 ^{ED}	0.490 ^{ED}
⁴ I _{9/2}	12401	52.13	0.456	0.393 ^{ED}	0.455 ^{ED}	0.476 ^{ED}
⁴ F _{9/2}	15148	194.37	2.548	2.434 ^{ED}	2.509 ^{ED}	2.534 ^{ED}
⁴ S _{3/2} + ² H _{11/2}	18686	665.59	13.660	13.399 ^{ED}	13.315 ^{ED}	13.655 ^{ED}
⁴ F _{7/2}	20315	72.60	1.705	1.869 ^{ED}	1.581 ^{ED}	1.739 ^{ED}
⁴ F _{5/2} + ⁴ F _{3/2}	22075	25.87	0.716	0.770 ^{ED}	0.530 ^{ED}	0.699 ^{ED}
² G _{9/2}	24435	21.27	0.719	0.672 ^{ED}	0.529 ^{ED}	0.659 ^{ED}
⁴ G _{11/2} + ² K _{15/2} + ⁴ G _{9/2} + ² G _{7/2}	26286	753.62	29.698	29.750 ^{ED} + 0.070 ^{MD}	29.781 ^{ED} + 0.070 ^{MD}	29.622 ^{ED} + 0.070 ^{MD}
<i>r.m.s. dev.</i>				0.175	0.181	0.038

* $\langle E \rangle$ - "center of gravity" of the absorption band, Γ – integrated absorption coefficient, f_{exp} and f_{calc} – experimental and calculated absorption oscillator strengths, respectively, ED and MD stand for electric-dipole and magnetic dipole contributions, respectively.

**Excluding the ⁴I_{15/2} → ⁴I_{13/2} transition from the fit.

Table 2. Intensity parameters for Er³⁺ ions in (Lu,Sc)₂O₃ ceramic.

Parameter	Value (theory)		
	J-O	J-O*	ICI*
Ω_2 , 10 ⁻²⁰ cm ²	7.151	7.048	7.267
Ω_4 , 10 ⁻²⁰ cm ²	1.646	1.919	1.784
Ω_6 , 10 ⁻²⁰ cm ²	0.783	0.539	0.664
R_2 , 10 ⁻⁴ cm			-0.012
R_4 , 10 ⁻⁴ cm			-0.084
R_6 , 10 ⁻⁴ cm			0.168

*Excluding the ⁴I_{15/2} → ⁴I_{13/2} transition from the fit.

Table 3. Emission probabilities* for Er³⁺ ions in (Lu,Sc)₂O₃ ceramic calculated within the ICI approximation.

Transition	$\langle\lambda\rangle$, nm	$A_{\text{calc}}^{\Sigma}(\text{JJ}')$, s ⁻¹	$B(\text{JJ}')$	A_{tot} , s ⁻¹	τ_{rad} , ms	
⁴ I _{13/2} →	⁴ I _{15/2}	1533	89.29 ^{ED} +69.92 ^{MD}	1	159.21	6.28
⁴ I _{11/2} →	⁴ I _{13/2}	2688	24.96 ^{ED} +16.56 ^{MD}	0.199	208.50	4.80
	⁴ I _{15/2}	976.1	166.98 ^{ED}	0.801		
⁴ I _{9/2} →	⁴ I _{11/2}	4515	1.30 ^{ED} +2.22 ^{MD}	0.010	338.38	2.96
	⁴ I _{13/2}	1685	46.79 ^{ED}	0.138		
	⁴ I _{15/2}	802.6	288.07 ^{ED}	0.852		
⁴ F _{9/2} →	⁴ I _{9/2}	3650	8.53 ^{ED} +4.12 ^{MD}	0.005	2522.8	0.40
	⁴ I _{11/2}	2018	89.38 ^{ED} +10.17 ^{MD}	0.039		
	⁴ I _{13/2}	1153	128.20 ^{ED}	0.051		
	⁴ I _{15/2}	657.9	2282.4 ^{ED}	0.905		
⁴ S _{3/2} +	⁴ F _{9/2}	3189	60.20 ^{ED} +0.28 ^{MD}	0.003	18221.5	0.055
² H _{11/2} →	⁴ I _{9/2}	1702	279.87 ^{ED} +1.19 ^{MD}	0.015		
	⁴ I _{11/2}	1236	179.07 ^{ED} +14.53 ^{MD}	0.011		
	⁴ I _{13/2}	846.7	762.60 ^{ED} +120.76 ^{MD}	0.049		
	⁴ I _{15/2}	545.4	16803.8 ^{ED}	0.922		

$\langle\lambda\rangle$ - mean emission wavelength, $A_{\text{calc}}^{\Sigma}(\text{JJ}')$ - probability of spontaneous transition (ED and MD stand for electric and magnetic dipole contributions, respectively), $B(\text{JJ}')$ - luminescence branching ratio, A_{tot} and τ_{rad} - total probability of spontaneous transitions from an excited-state and its radiative lifetime, respectively.

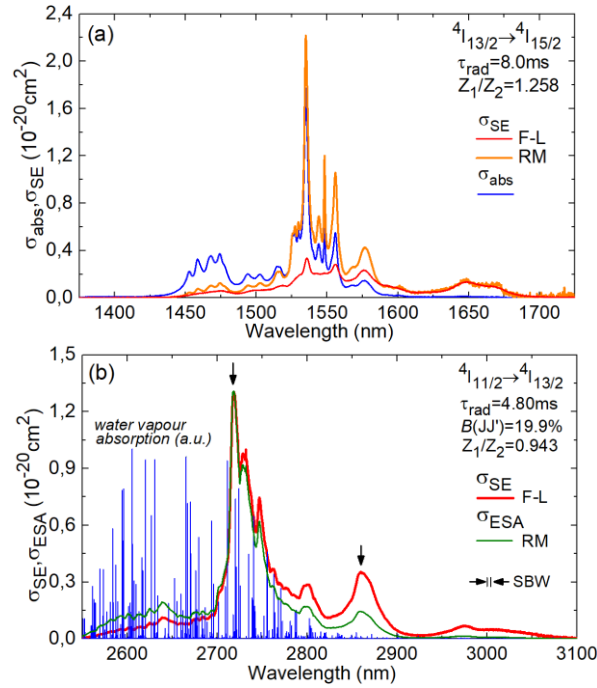


Fig. 6. RT stimulated-emission cross-sections, σ_{SE} , for Er^{3+} ions in $(\text{Lu},\text{Sc})_2\text{O}_3$ ceramic: (a) the $4I_{13/2} \rightarrow 4I_{15/2}$ transition and (b) the $4I_{11/2} \rightarrow 4I_{13/2}$ transition. F-L - Füchtbauer-Ladenburg equation, RM – reciprocity method. *Blue spectrum* in (b) – water vapor absorption in the atmosphere (from Hitran database). In (a), the σ_{abs} spectrum is given for comparison. In (b), the σ_{ESA} spectrum ($4I_{13/2} \rightarrow 4I_{11/2}$) is calculated. *Arrows* indicate the observed laser lines.

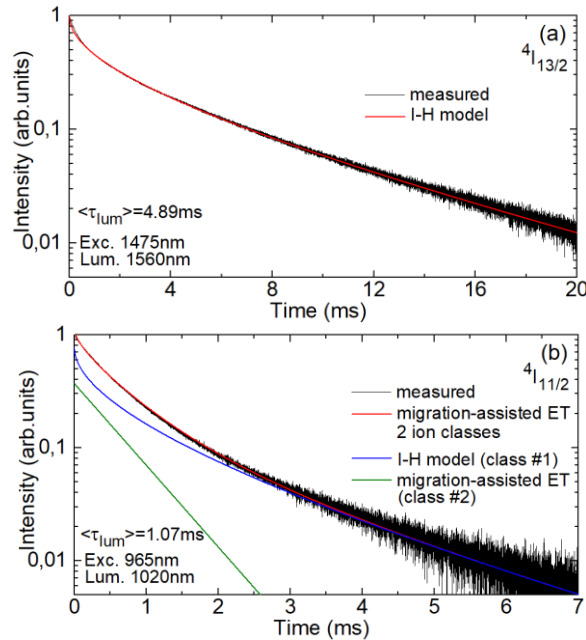


Fig. 7. RT luminescence decay curves for 7 at.% $\text{Er}:(\text{Lu},\text{Sc})_2\text{O}_3$ ceramic: (a) the $4I_{13/2}$ state, $\lambda_{exc} = 1475$ nm, $\lambda_{lum} = 1560$ nm. *Black curve* – measured decay, *red curve* – its fitting using the Inokuti-Hirayama (I-H) model; (b) the $4I_{11/2}$ state, $\lambda_{exc} = 965$ nm, $\lambda_{lum} = 1020$ nm. *Black curve* – measured decay, *red curve* – its fitting using the model of migration-assisted energy-transfer and two ions classes, *blue* and *green curves* – ion class #1 and #2, $\langle \tau_{lum} \rangle$ - average luminescence lifetime.

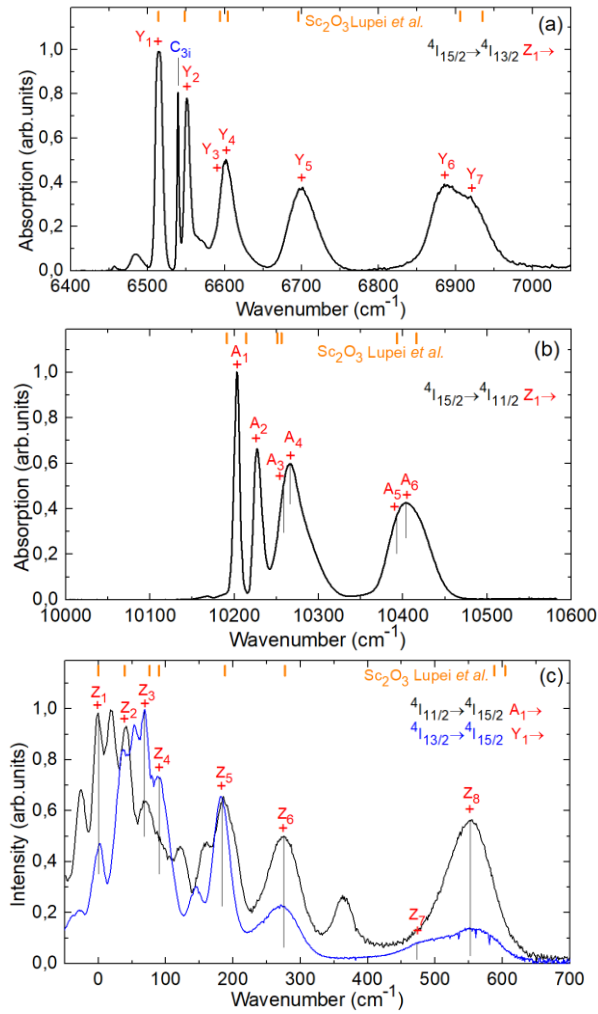


Fig. 8. LT (12 K) spectroscopy of Er^{3+} ions in $(\text{Lu},\text{Sc})_2\text{O}_3$ ceramic: (a,b) absorption spectra: (a) the ${}^4I_{15/2} \rightarrow {}^4I_{13/2}$ transition, (b) the ${}^4I_{15/2} \rightarrow {}^4I_{11/2}$ transition; (c) emission spectra for the ${}^4I_{11/2} \rightarrow {}^4I_{15/2}$ and ${}^4I_{13/2} \rightarrow {}^4I_{15/2}$ transitions. Z_i ($i = 1 \dots 8$), Y_j ($j = 1 \dots 7$) and A_k ($k = 1 \dots 6$) number the Stark sub-levels of the ${}^4I_{15/2}$, ${}^4I_{13/2}$ and ${}^4I_{11/2}$ multiplets, respectively, for C_2 sites. C_{3i} in (a) – lines assigned to MD transitions for C_{3i} sites. Orange dashes – crystal-field splitting for Er^{3+} in C_2 sites in Sc_2O_3 [37].

Table 4. Crystal-field splitting for Er³⁺ ions in C₂ sites in (Lu,Sc)₂O₃ ceramic. The empirical notations of the multiplets are after [39].

Manifold	Notation	Stark components (cm ⁻¹)
⁴ I _{15/2}	Z	0, 41, 68, 90, 184, 275, 473, 552
⁴ I _{13/2}	Y	6514, 6551, 6596, 6600, 6699, 6887, 6919
⁴ I _{11/2}	A	10203, 10227, 10258, 10266, 10393, 10404
⁴ I _{9/2}	B	12303, 12439, 12523, 12600, 12630
⁴ F _{9/2}	D	15109, 15191, 15292, 15330, 15467
⁴ S _{3/2}	E	18201, 18309
² H _{11/2}	F	19049, 19233, 19307 (3 missing)
⁴ F _{7/2}	G	20322, 20467, 20496, 20607
⁴ F _{5/2}	H	22050, 22179 (1 missing)
⁴ F _{3/2}	I	22398, 22589
² H _{9/2}	K	24337, 24554, 24614 (2 missing)
⁴ G _{11/2}	L	26137, 26448 (4 missing)

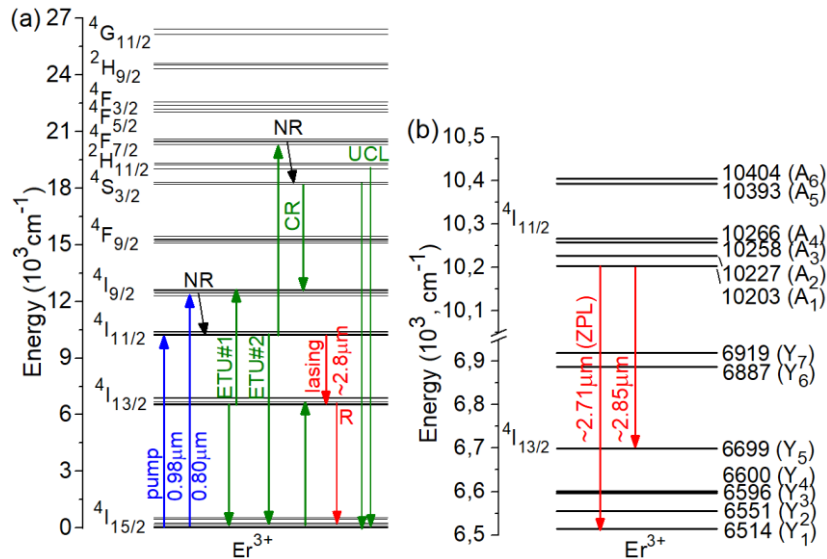


Fig. 9. Scheme of energy-levels of Er³⁺ ions in C₂ sites in (Lu,Sc)₂O₃ ceramic: (a) general scheme: *blue and red arrows* – pump and laser transitions, respectively, ETU – energy-transfer upconversion, CR – cross-relaxation, R and NR – radiative and non-radiative transitions, respectively, UCL – upconversion luminescence; (b) splitting of the ⁴I_{11/2} and ⁴I_{13/2} multiplets, *arrows* – observed laser lines.

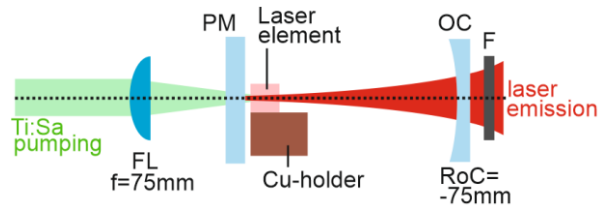


Fig. 10. Scheme of the $\text{Er}:(\text{Lu},\text{Sc})_2\text{O}_3$ ceramic laser: FL – focusing lens, PM – pump mirror, OC – output coupler, F – long-pass filter.

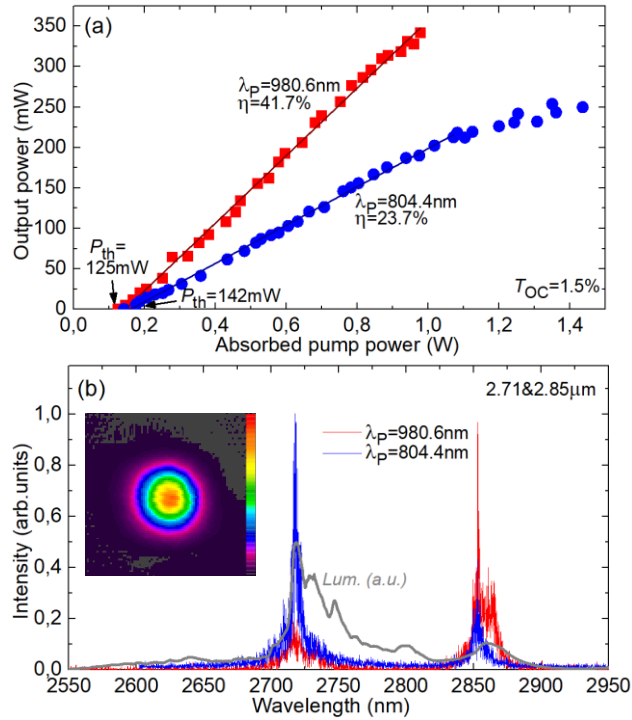


Fig. 11. $\text{Er}:(\text{Lu},\text{Sc})_2\text{O}_3$ ceramic laser: (a) input-output power dependences for $\lambda_P = 804.4$ nm and 980.6 nm, η – slope efficiency; (b) typical laser emission spectra, *inset* – spatial profile of the laser mode in the far-field. $T_{OC} = 1.5\%$. The laser emission is unpolarized. For comparison the luminescence curve is implemented (gray).

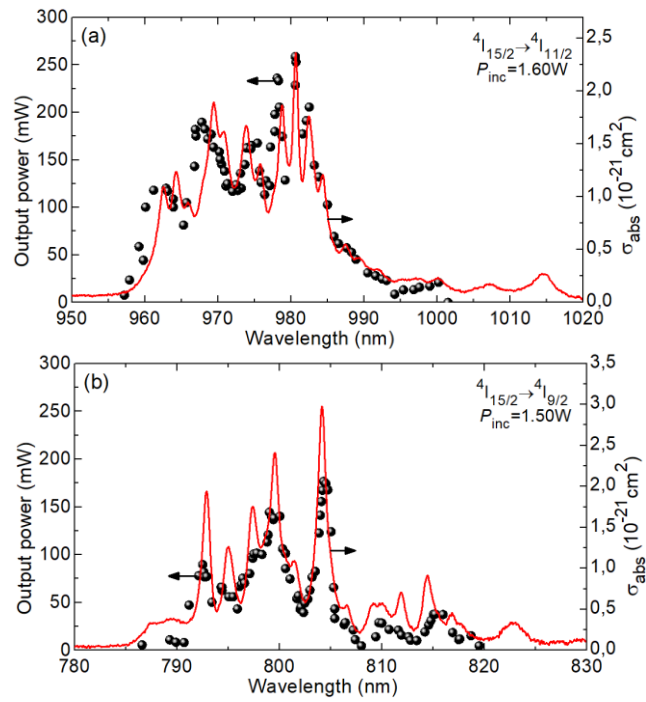


Fig. 12. Laser excitation curves for the Er:(Lu,Sc)₂O₃ ceramic laser (output power vs. the pump wavelength) measured at a fixed incident pump power P_{inc} : pumping into (a) the $^4I_{15/2}$ state and (b) the $^4I_{9/2}$ state. Symbols – laser output power, curves – σ_{abs} spectra.